CrossMark

A simulation study for estimating scatter fraction in whole-body ^{18}F-FDG PET/CT

Shota Hosokawa[1,2,5] · Kazumasa Inoue[1] · Daisuke Kano[3] · Fuminori Shimizu[4] ·
Kazuya Koyama[1,6] · Yoshihiro Nakagami[4,7] · Yoshihisa Muramatsu[4] ·
Masahiro Fukushi[1]

Abstract Whereas Monte Carlo (MC) simulation is widely utilized in estimation of the scatter component, a simulation model which can calculate the scatter fraction (SF) of each patient is needed for making an accurate image quality assessment for clinical PET images based on the noise equivalent count. In this study, an MC simulation model was constructed which can calculate the SF for various phantoms. We utilized the Geant4 toolkit based on MC simulation to make a model of a PET scanner with a scatter phantom, and SFs calculated with this model were compared with the SF (SF$_{constant}$: 44%) measured with use of an actual PET scanner. Additionally, the SF values for an anthropomorphic phantom were calculated from its voxel phantom. Furthermore, we evaluated the impact on the SF due to the difference in the source distribution inside the phantom. The SF calculated from the scatter phantom in the MC simulation was 44%, the same as the SF$_{constant}$ value. The average SF for the anthropomorphic phantom was 41%, but there was a maximum of 14 percentage points difference between each scan range, and the maximum difference in the SF was 8 percentage points for the difference in the source distribution. We constructed an MC simulation model which can calculate SFs for various phantoms. The SF was confirmed to be affected significantly by the source distribution. We judged that the actually measured SF$_{constant}$ obtained from the PET scanner with the scatter phantom was not suitable for the assessment of the quality of all patient images.

Keywords ^{18}F-FDG PET/CT · Scatter fraction · Noise equivalent count rate · Monte Carlo simulation · Voxel phantom · Geant4

✉ Kazumasa Inoue
kzminoue@tmu.ac.jp

1 Department of Radiological Sciences, Graduate School of Human Health Sciences, Tokyo Metropolitan University, 7-2-10 Higashiogu, Arakawa-ku, Tokyo 116-8551, Japan

2 Department of Radiation Oncology, National Cancer Center Hospital East, 6-5-1 Kashiwanoha, Kashiwa, Chiba 277-8577, Japan

3 Department of Pharmacy, National Cancer Center Hospital East, 6-5-1 Kashiwanoha, Kashiwa, Chiba 277-8577, Japan

4 Department of Diagnostic Radiology, National Cancer Center Hospital East, 6-5-1 Kashiwanoha, Kashiwa, Chiba 277-8577, Japan

5 Department of Radiation Science, Graduate School of Health Sciences, Hirosaki University, 66-1 Hon-cho, Hirosaki, Aomori 036-8564, Japan

6 Department of Radiological Sciences, Faculty of Radiological Sciences, Japan Health Care College, 434-1 Shin-ei, Kiyota-ku, Sapporo 004-0839, Japan

7 Yokohama City University School of Medicine Medical Course Radiology, 3-9 Fukuura, Kanazawa-ku, Yokohama 236-0004, Japan

1 Introduction

The image quality obtained from positron emission tomography (PET) depends on the performance of the scanner, and on an acquisition and an image reconstruction parameter. Thus, in clinical trials in which many institutes participate, the standardization of the acquisition and reconstruction parameters based on a physical indicator is necessary for correct determination of the utility of new radiopharmaceuticals. The noise equivalent count (NEC) [1–5] is widely utilized as a physical indicator for evaluating the PET image quality. The NEC is a value indicating the ratio of the true coincidence count which contributes to

the PET imaging. NEC$_{patient}$ [6] and NEC$_{density}$ [7] have also been suggested as physical indicators for the quality assessment of clinical images in a guideline from the Japanese Society of Nuclear Medicine (JSNM) and the Japanese Society of Nuclear Medicine Technology (JSNMT). The JSNM-JSNMT guideline [8] recommends that the physical indicators meet the criteria of NEC$_{patient}$ at >13 Mcounts/m and NEC density at >0.2 kcounts/cm^3.

It is necessary to know the exact scatter fraction (SF) for each patient to be able to calculate NEC$_{patient}$ and NEC$_{density}$ accurately. However, it is impossible to measure the scatter coincidence count directly using any currently available PET scanners because none is able to discriminate among the differences in the incident energy. This is because there is a limitation on the energy resolution of the scintillators that are utilized for current PET scanners [9]. Therefore, the energy window has been set to about 511 keV $\pm$ 25% for PET scanners containing $Bi_4Ge_3O_{12}$ (BGO) crystals [10] with an energy resolution of 18% [11].

The NEMA NU 2-2007 Standards Publication [12] sets use of a scatter phantom with a diameter of 20 cm and length of 70 cm, and a line source for calculating the SF (SF$_{constant}$). The SF$_{constant}$ is given by calculation of the ratio of the scatter coincidence count that is obtained from interpolation processing on a sinogram to the prompt coincidence count. However, it is impossible to calculate the SF accurately by applying the above method to clinical images which exhibit a complex source distribution. In previous reports about the quality assessment of clinical images based on the NEC, the SF$_{constant}$ obtained from a scatter phantom was utilized as an alternative value because there is no solution to the above problem [13–18]. In a previous report [13], it was stated that the PET image quality could possibly be kept at a certain level for different body types by adjustment of the acquisition time based on the NEC$_{density}$. However, the correlation between the result of a visual assessment of image quality and the body mass index (BMI) of a patient is extremely low. This is due to the use of the SF$_{constant}$ obtained from the scatter phantom for clinical data; this uncertainty is described in the JSNM-JSNMT guideline [8].

Monte Carlo (MC) simulation is widely utilized for estimation of scattering rays in the medical, engineering, and nuclear fields. Although such a simulation can also be used for calculating the SF, it is necessary to consider the cross-sectional area of patient's body and the source distribution inside the body of each patient for calculation of an accurate SF, because these factors influence the SF [19, 20]. Constantinescu and Mukherjee [21] estimated the SF of a rat and mouse by assuming their body types to be cylinders for the MC simulation. Konik et al. [20] also estimated the SF of a cylindrical phantom with different diameters and an anthropomorphic phantom (XCAT).

However, it is still necessary to create an individual simulation model to estimate the SF of each imaging target.

In this study, we initially created a voxel phantom based on the Hounsfield units obtained from a CT image by taking advantage of the high operating rate of a PET/CT scanner in a clinical PET examination. An MC simulation model that can calculate the SF using the voxel phantom was then constructed. Additionally, the SF is known to be affected not only by the cross-sectional area of the object, but also by the source distribution inside the object. Therefore, we evaluated the impact on the SF due to the difference in the source distribution by use of a cylindrical phantom.

2 Materials and methods

2.1 Construction of MC simulation model

A Discovery ST (GE Healthcare, Milwaukee, WI, USA) PET/CT scanner was used in this study. This scanner has $Bi_4Ge_3O_{12}$ (bismuth germinate: BGO) crystals with dimensions of 6.3 mm $\times$ 6.3 mm $\times$ 30 mm in the tangential, axial, and radial directions, respectively. The transaxial and axial fields of view (FOVs) are 700 and 151.2 mm, respectively. The 3D scan mode was used for the PET scan. The energy window was set to 375−650 keV. The tube voltage was set to 120 kV, and the tube current was determined by an auto exposure control with a noise index of 10 for the CT scan. The matrix size of the reconstructed CT image was set to 512 $\times$ 512. A Geant4 (ver. 10.0) toolkit was used for MC simulation [22]. This toolkit is able to simulate the passage of particles through matter and is widely utilized in various research fields [23–25]. The MC simulation model was made based on the example code (geant4/examples/extended/medical/DICOM) for Geant4. The calculation conditions were not changed because this example code was prepared for medical applications. G4EmStandardPhysics was used for electro-magnetic process. The detector part was constructed for the MC simulation based on the PET/CT scanner specifications (Fig. 1). Recent commercially available PET/CT scanners have an end shield outside the detector to reduce the scatter coincidence count from the outside of the field of view. However, the Discovery ST was not equipped with such an end shield. Thus, it was not considered here. The geometry of a PET/CT scanner bed was made from the CT scan data (i.e., DICOM data set) [26]. A general-purpose personal computer (CPU, Intel® Core™2 Duo; frequency, 3.33 GHz; memory, 3.6 GB; OS, Scientific Linux 64 bits) was used for the MC simulation. In the simulation model that we developed, positrons were not used for the generating particles. Instead, we used two

annihilation radiations with an energy of 511 keV to save calculation time. The number of trials for the MC simulation was set to 1×10^8 times. The energy resolution (18%) of the PET scanner was reproduced by multiplying the coefficient that was decided on as a random number by the energy deposited into a BGO crystal. In the deposited energy that we obtained, the photons with energy of $375-650$ keV were set as the coincidence count. If a photon was scattered inside the scintillator, the line of response (LOR) was decided by calculation of the weighted center from each center position of the scintillator based on the deposited energy. The decision about the coincidence count was made for every particle event to ignore the presence of the random coincidence count [27] and multi-hit event. The projection data obtained were sorted as a transaxial 2D sinogram by the single-slice rebinning method [28]. We used four types of phantoms (Fig. 2).
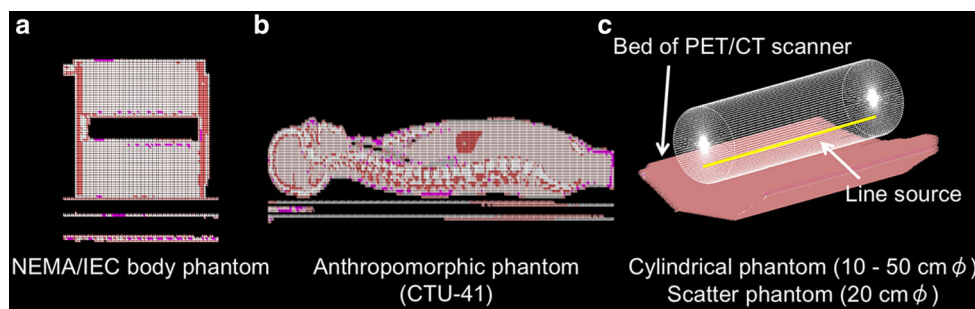
2.2 Calculations of SFs for cylindrical phantoms

In the NEMA NU 2-2007 Standards Publication [12], the sinogram that was projected for one sine wave obtained by the scatter phantom with the line source was used for
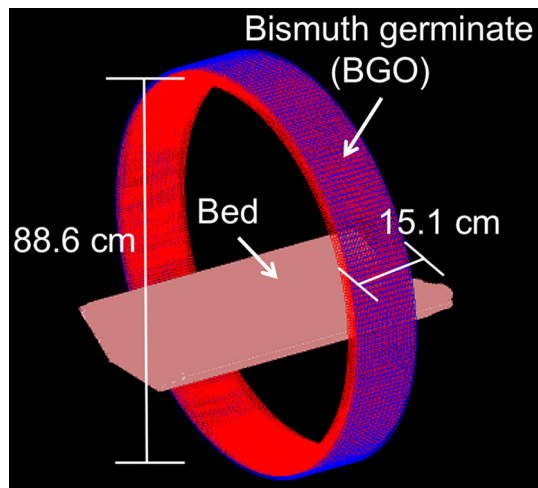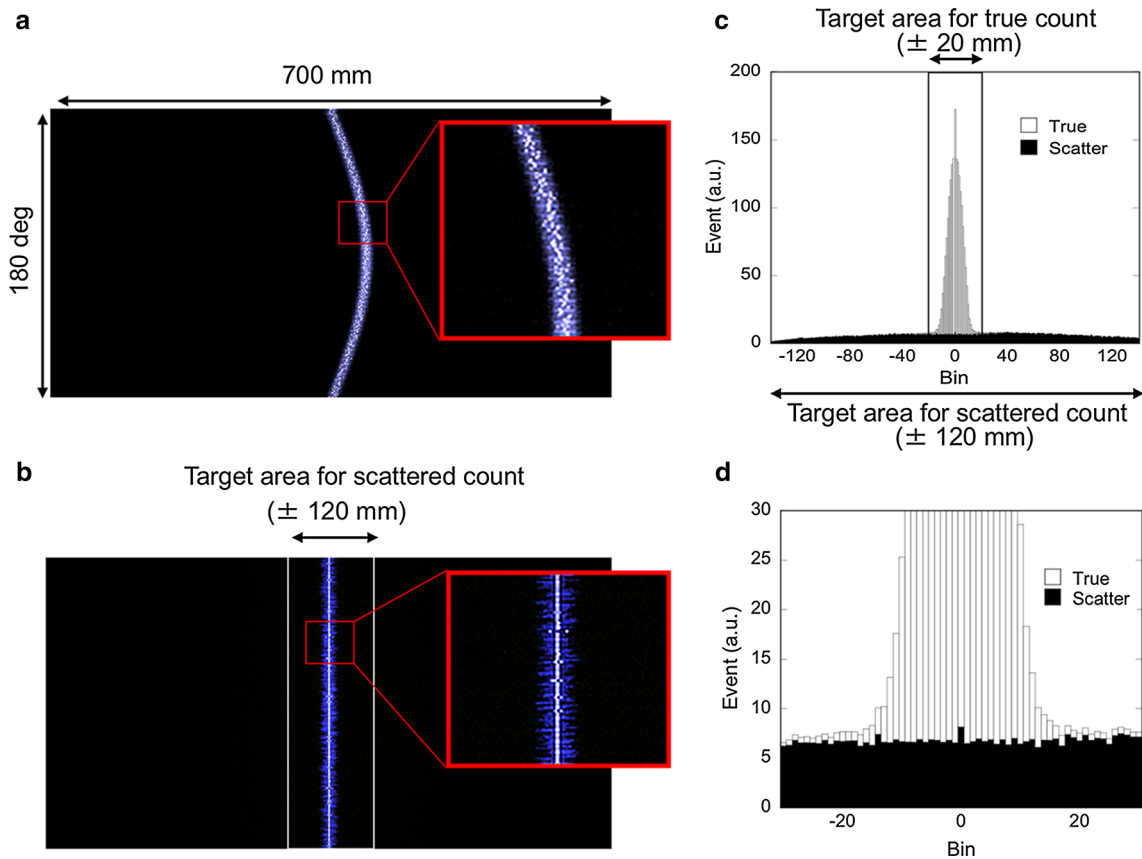

Fig. 1 A model in the Monte Carlo simulation for a PET scanner

calculation of the $SF_{constant}$ (Fig. 3a). Each projection in the sinogram is shifted so that the peak of the projection is aligned with the center of the sinogram (Fig. 3b). This produces a sum projection with a count density distribution around the peak for the maximum counts at the center of the sinogram (Fig. 3c, d). If two or more maximum pixels were detected at each row of the sinogram, each row was shifted to the center of the sinogram based on the middle position of these maximum pixels. The scattered counts were defined by linear interpolation at ± 20 mm within ± 120 mm length from the maximum value as shown in Fig. 3c, and $SF_{constant}$, which is the ratio of scatter coincidence counts to prompt coincidence counts, was calculated. Thus, the count obtained was discriminated as a scattered count when the LOR was obtained ± 20 mm or more away from the original source position.

It is impossible to estimate by the above method the scattered count from a sinogram of a patient that has an intricate source distribution. However, the estimation is possible with the use of MC simulation because information such as the distance from the LOR and the original source position can be obtained easily. In this study, using MC simulation, we calculated three SFs ($SF_{direct-NEMA}$, $SF_{interpolation-NEMA}$, and $SF_{direct-all}$) with different definitions (i.e., different target areas for true and scattered count evaluations) for a cylindrical phantom (Table 1). We calculated the $SF_{direct-NEMA}$ directly by checking whether the photon was scattered during the calculation process of the MC simulation. The $SF_{interpolation-NEMA}$ was also calculated by interpolation processing on the sinogram. The sinogram was made based on the MC simulation results. Only the counts that are detected within ± 120 mm distance from the source position are targeted for the SF calculation in the NEMA NU 2-2007 Standards Publication, but all the counts that are detected at more than ± 120 mm distance from the source position are targeted in actual clinical PET/CT examinations. Thus, $SF_{direct-all}$ was calculated by targeting the whole area of the FOVs (i.e., inside and outside FOVs) for evaluating the scattered count. All the SFs obtained were compared to the actually measured $SF_{constant}$ of the scatter phantom obtained with use of the PET/CT scanner. The densities of the scatter phantom and the bed

Fig. 2 The NEMA/IEC body phantom (**a**), the anthropomorphic phantom (**b**), and the cylindrical phantom or scatter phantom (**c**) with the bed of the PET/CT scanner

Fig. 3 A sinogram obtained for a scatter phantom with a line source (**a**). Each projection in the sinogram is shifted so that the peak of the projection is aligned with the center of the sinogram (**b**) for interpolation processing according to the NEMA NU 2-2007 Standards Publication [12] (**c**). **d** An enlarged view of part of **c**

Table 1 Definition of target area for evaluating true and scatted counts for calculating the scatter fraction (SF)

SF	Target area for true count from original source position (mm)[a]	Target area for scatted count from original source position (mm)[b]	Calculation method
$SF_{constant}$	$<\pm20$	$<\pm120$	Actual measured value
$SF_{direct\text{-}NEMA}$	$<\pm20$	$<\pm120$	MC simulation
$SF_{interpolation\text{-}NEMA}$	$<\pm20$	$<\pm120$	MC simulation
$SF_{direct\text{-}all}$	$<\pm20$	$<\pm700$	MC simulation

[a] The target area is defined according to Fig. 3c

[b] The target area is defined according to Fig. 3a, b

of the PET/CT scanner (HU: −900) were set to 0.96 and 0.26 g/cm^3, respectively [26].

The same calculations as described above for the SFs of the scatter phantom were performed by use of a cylindrical phantom with different diameters, 10–50 cm, for evaluation of the dependence of phantom sizes for SFs. For all size diameters of the cylindrical phantom, the ratio of the distance between the center of the phantom and the line source to that between the line source and the edge of the phantom was set as 4.5–5.5.

2.3 Impact on $SF_{direct\text{-}all}$ by the ellipticity and the source distribution

In actual clinical PET/CT examinations, the cross-sectional area and the source distribution inside the body of each patient differ depending on the patient's body type and the presence of subcutaneous fat. Therefore, we calculated the $SF_{direct\text{-}all}$ by changing the ellipticity (0–75%) based on a cylindrical phantom with a diameter of 20 cm so that sources were distributed everywhere equally, as shown in

Fig. 4a. The ellipticity (El) is defined in Eq. (1). In addition, SF$_{direct-all}$ was calculated from changes in the source distribution ratio (1–100%) based on a phantom with a diameter of 20 cm and an ellipticity of 0%, as shown in Fig. 4b:

$$\mathrm{El} = \frac{D_{major} - D_{minor}}{D_{major}} \times 100 \ (\%), \qquad (1)$$

where D_{major} and D_{minor} are the major and minor axes of the elliptical cylindrical phantom.

2.4 Calculation of SF$_{direct-all}$ of anthropomorphic and NEMA/IEC body phantoms

The SF$_{direct-all}$ was calculated for an anthropomorphic phantom with a volume of 36,004 cm^3 and a length of 65.4 cm (CTU-41, Kyoto Kagaku Co., Ltd., Kyoto, Japan) and the NEMA/IEC body phantom. We constructed voxel phantoms for the simulation model by performing a CT scan with both phantoms. The Hounsfield units obtained from the CT scan were first converted to density and then converted to the material according to ICRU Report 46 [29] for the MC simulation.

For the calculation of SF$_{direct-all}$ of the anthropomorphic phantom, the PET scan length was set from the lower edge of the cerebellum to the top of the bladder, as shown in Fig. 5. The source was positioned uniformly inside the phantom, including the lung region. The length for the simulation was set to 151.2 mm, which was the same as for the actual PET/CT scanner, and SF$_{direct-all}$ was calculated for each region.
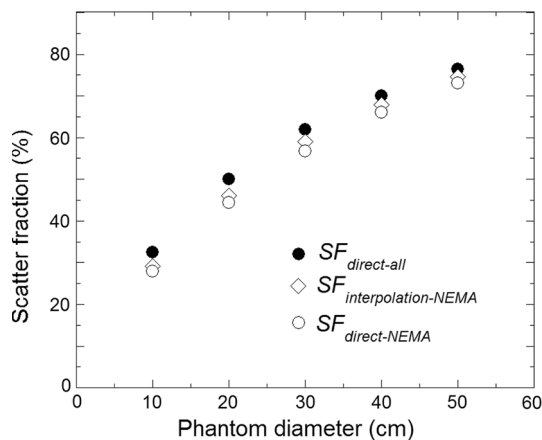
For the calculation of SF$_{direct-all}$ of the NEMA/IEC body phantom, all the spheres were set in the NEMA/IEC body phantom so that the sphere centers were located on a single plane parallel to the transaxial center slice. The source was positioned uniformly inside the body phantom. In the case of scanning of the NEMA/IEC body phantom, the JSNM-JSNMT guideline [8] recommends the use of the scatter phantom to reproduce scattering of rays from outside the FOVs, but it does not enforce its use. Therefore, we calculated SF$_{direct-all}$ of the NEMA/IEC body phantom with and without the scatter phantom.

Fig. 4 The cylindrical phantom with different ellipticties (**a** 0–75%) and source distribution ratios (**b** 1–100%). The distributed source area is represented in *yellow* (color figure online)
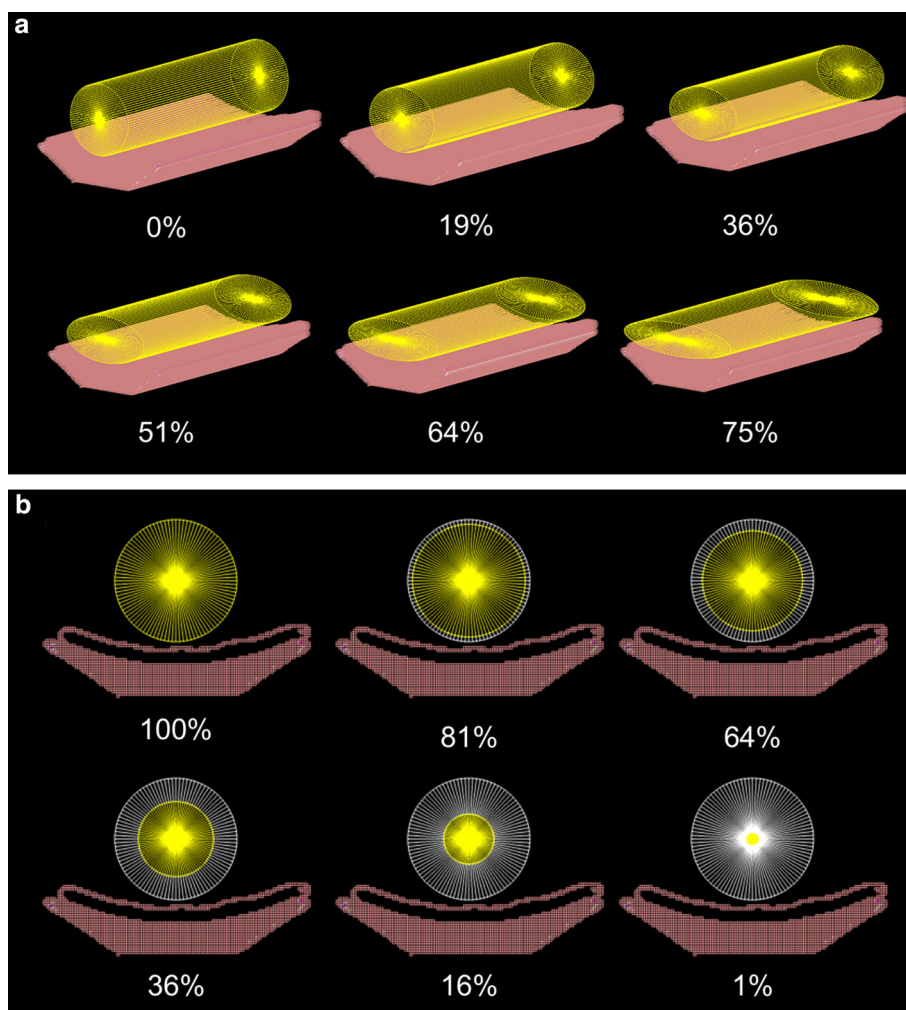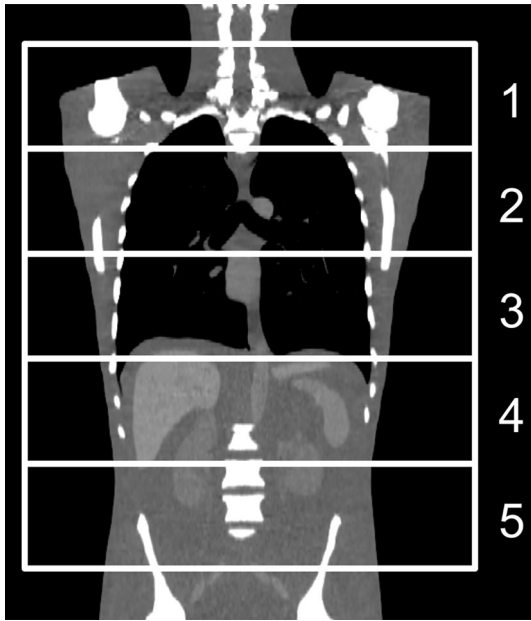
Fig. 5 The simulation area on an anthropomorphic phantom. The axial length of the simulation area was divided into five regions according to the specifications of the actual PET/CT scanner

Fig. 6 Correlation between cylindrical phantom diameter and calculated SF

3 Results

3.1 Calculations of SFs for cylindrical phantom

The calculated $SF_{direct-NEMA}$, $SF_{interpolation-NEMA}$, and $SF_{direct-all}$ of the cylindrical phantom with diameters of 10–50 cm are shown in Fig. 6. The calculated SFs increased as the phantom diameter increased, but the increase was not linear. The $SF_{direct-NEMA}$ and $SF_{interpolation-NEMA}$ at a cylindrical phantom diameter of 20 cm (i.e., the scatter phantom) were 44 and 46%, respectively, and a value of 44% was obtained for $SF_{constant}$, which is the actually measured value for the PET/CT scanner [30]. Although all $SF_{interpolation-NEMA}$ values were higher than those of $SF_{direct-NEMA}$, the maximum difference was 2 percentage points when the diameter of the cylindrical phantom was 30 cm. The $SF_{direct-all}$ for the cylindrical phantom diameter of 20 cm (i.e., the scatter phantom) was 50%; this was higher compared to the above SFs.

3.2 Impact on $SF_{direct-all}$ by the ellipticity and the source distribution

The $SF_{direct-all}$ values calculated from the cylindrical phantom with different ellipticties and source distribution ratios inside the phantom are shown in Fig. 7. The $SF_{direct-all}$ decreased from 44 to 37% when the ellipticties were changed from 0 to 75% for the same length and volume of the phantom (Fig. 7a). Additionally, the calculated $SF_{direct-all}$ increased from 44 to 52% when the source distribution ratio was changed from 100 to 1% (Fig. 7b).

3.3 Calculation of $SF_{direct-all}$ of anthropomorphic and NEMA/IEC body phantoms

Table 2 shows the calculated $SF_{direct-all}$ at each scanner bed position, obtained for the anthropomorphic phantom (CTU-41). The average $SF_{direct-all}$ was 41%. This result was lower than that for $SF_{constant}$ (44%), which was obtained by use of the scatter phantom. The true coincidence count per volume (counts/cm^3) had a maximum of two-fold difference, depending on the phantom region. The calculated $SF_{direct-all}$ values obtained for the NEMA/IEC body phantom with and without the scatter phantoms were 43 and 39%, respectively, resulting in a percentage point difference of 4. In addition, the calculated $SF_{direct-all}$ value for the scatter phantom was the same as that of $SF_{constant}$, whereas the calculated $SF_{direct-all}$ value without the scatter phantom was 5 percentage points lower than that of $SF_{constant}$.

4 Discussion

4.1 Calculation of SFs for cylindrical phantom

The $SF_{direct-NEMA}$, $SF_{interpolation-NEMA}$, and $SF_{direct-all}$ of the cylindrical phantom with different diameters were calculated by MC simulation. The calculated SFs increased when the phantom diameter was increased, but the increases were not linear because the ratio of attenuation of the annihilation gamma rays inside the phantom increased. This result was consistent with that previously reported [31]. Also, Konik et al. [20] reported that the SF for the scatter phantom with a 50 cm diameter had a 1.5 times higher value than that for a 20 cm diameter phantom. The present result, as shown in Fig. 6, was consistent with the finding of Konik et al. [20].

Fig. 7 Correlation between ellipticity and SF (**a**), and between source distribution ratio and SF (**b**)
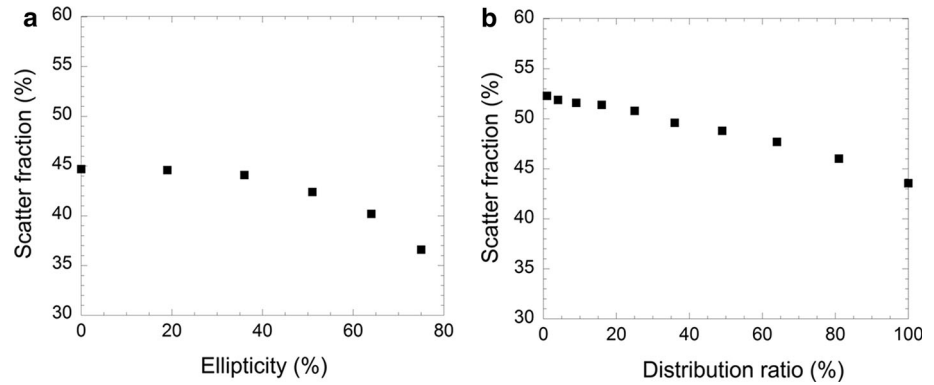
Table 2 Calculated scatter fraction ($SF_{direct-all}$) obtained for the anthropomorphic phantom (CTU-41)

Region no.	Region	$SF_{direct-all}$ (%)	Volume (cm^3)	True/volume (counts/cm^3)	Scatter/volume (counts/cm^3)
1	Neck	44	3.14×10^3	16.8	13.2
2	Upper chest	36	8.39×10^3	15.8	8.9
3	Lower chest	34	9.13×10^3	19.5	10.1
4	Upper abdomen	48	7.74×10^3	9.9	9.1
5	Lower abdomen	45	7.61×10^3	10.0	8.2
	Average	41	7.20×10^3	14.4	9.9

The calculated $SF_{interpolation-NEMA}$ was higher than that of $SF_{constant}$. In this study, the true count for $SF_{interpolation-NEMA}$ was defined as that which was not scattered with the object and detected within ± 20 mm from the LOR to the source position (Fig. 3c). However, the true count was detected at ± 20 mm or more positions from the center of the sinogram, as shown in Fig. 3d, because the number of calculation trials was insufficient, resulting in a variation of the maximum value of each line on the sinogram (white points in Fig. 3a, b), and we had overestimated $SF_{interpolation-NEMA}$ compared to $SF_{constant}$. On the other hand, $SF_{direct-NEMA}$, which targeted the area exceeding ± 20 mm (i.e., ± 120 mm) for the true count, was exactly the same as $SF_{constant}$, and we confirmed the credibility of this MC simulation model.

Studies using MC simulation have a trade-off relationship between accuracy and calculation time, and the practical number of calculation trials is limited. We set the number of calculation trials that could be finished within 6 h as our limit (e.g., 1.0×10^8 for the cylindrical phantom with 20 cm diameter). Thus, the calculation accuracy for $SF_{interpolation-NEMA}$ that needs interpolation processing depends on the number of calculation trials, whereas the calculation accuracy of $SF_{direct-NEMA}$ is independent of the number of calculation trials because interpolation processing is not required. Therefore, the value of $SF_{direct-NEMA}$ converged quickly. In fact, the calculated $SF_{direct-NEMA}$ for the cylindrical phantom with 20 cm diameter

(i.e., the scatter phantom) agreed with $SF_{constant}$ (44%). This calculation of $SF_{direct-NEMA}$ was possible within a realistic time.

In the calculation method based on the NEMA NU 2-2007 Standards Publication, the target area for the scattered count is limited to $< \pm 120$ mm from the original source position because the SF obtained depends on the size of the FOVs. Therefore, the defined $SF_{direct-NEMA}$ is suitable for estimating the performance of PET/CT scanners by MC simulation; however, it is not suited for a quality assessment of clinical images based on the NEC because the effect due to differences in the specifications of PET/CT scanners must be considered when the SF is calculated. In addition, the interpolation processing of the sinogram which was defined in the NEMA NU 2-2007 Standards Publication cannot be used for the quality assessment of clinical images because multiple sine waves are mixed in the sinogram obtained from a patient. Therefore, $SF_{direct-all}$ was defined in a way that removed the limitation of the target area for the scattered count to resolve those issues. The $SF_{direct-all}$ calculated for the cylindrical phantom with 20 cm diameter (i.e., the scatter phantom) (50%) was 6 percentage points higher compared to $SF_{direct-NEMA}$ (44%), as shown in Fig. 6. Those differences corresponded to the scattered count obtained from outside the targeted area that was defined in the NEMA NU 2-2007 Standards Publication (i.e., $> \pm 120$ mm from the original source position).

We confirmed the validity of the developed MC simulation model and the calculated SFs, and the usefulness for the quality assessment of clinical images in the above discussions. For a more detailed evaluation, the $SF_{direct-all}$ was then calculated by changing the ellipticity and the source distribution of the cylindrical phantom with 20 cm diameter for the same length and volume (Fig. 7). The cycloid type phantom had a small ellipticity and a small source distribution ratio, and the $SF_{direct-all}$ obtained tended to increase, whereas the leptosome type phantom had large ellipticity and a large source distribution ratio, and the $SF_{direct-all}$ tended to decrease. Based on these results, both factors must be considered when an accurate $SF_{direct-all}$ is to be calculated by MC simulation.

4.2 Calculation of $SF_{direct-all}$ of anthropomorphic and NEMA/IEC body phantoms

The average $SF_{direct-all}$ calculated for the anthropomorphic phantom (CTU-41) was 41%; this result was 3 percentage points lower than that calculated from $SF_{constant}$ with a cylindrical phantom having a diameter of 20 cm (i.e., the scatter phantom). This $SF_{direct-all}$ value was calculated when the source was uniformly distributed. In an actual clinical situation, the source distribution tends to place a disproportionate emphasis on the deep parts of the human body. If a patient has a body type similar to that of the anthropomorphic phantom, the calculated $SF_{direct-all}$ (41%) will be increased due to a bias of the source distribution, resulting in $SF_{constant}$ (44%) being close to the value obtained for the PET/CT scanner. For example, for an average Japanese woman [32] who has a weight of 58 kg, an abdominal girth of 82 cm, and a subcutaneous fat region of the abdomen of 193 cm^2, the source distribution ratio is estimated to be 64% if the body type is assumed to be a cylindrical phantom. The calculated $SF_{direct-all}$ was estimated to be 45% based on the result in Fig. 7. From this, we see that the use of $SF_{constant}$ is a reasonable approach to the assessment of image quality for the standard body type of a patient. However, it is an unsuitable approach to use a constant $SF_{constant}$ (44%) calculated from the scatter phantom for all kinds of body types. In fact, the maximum calculated $SF_{direct-all}$ for an anthropomorphic phantom was 14 percentage points different depending on the scanner bed position (Table 2), and this result suggests that the $SF_{direct-all}$ can differ widely depending on the body type.

In the image quality assessment by use of the NEMA/IEC body phantom, we evaluated the impact from the presence of the scatter phantom which was placed outside the FOV. When the scatter phantom was placed outside the FOV, the calculated $SF_{direct-all}$ increased from 39 to 43%, resulting in a value similar to that of $SF_{constant}$ (44%), that is, the simulated value for the average body type. Thus, use

of the scatter phantom is a suitable approach to image quality assessment for evaluating PET/CT acquisition and image reconstruction parameters.

5 Conclusion

We could construct an MC simulation model which can calculate the SF for all kinds of body types using a voxel phantom. This model is useful for current clinical situations because the voxel phantom can be constructed easily by use of CT images which were obtained from PET/CT examination. In the image quality assessment using the NEMA/IEC body phantom with a scatter phantom, the use of $SF_{constant}$ (44%) for the standard body type was a suitable approach to the assessment of the clinical image quality; however, it was not suitable for all kinds of body types because the SF depends significantly on the object size and the source distribution. The MC simulation model which we constructed is expected to improve the accuracy of the NEC.

References

1. Strother SC, Casey ME, Hoffman EJ. Measuring PET scanner sensitivity: relating count rates to image signal-to-noise ratios using noise equivalent counts. IEEE Trans Nucl Sci. 1990;37:783–8.
2. Adam LE, Karp JS, Daube-Witherspoon ME, Smith RJ. Performance of a whole-body PET scanner using curve-plate NaI(Tl) detectors. J Nucl Med. 2001;42:1821–30.
3. Watson CC, Casey ME, Beyer T, Bruckbauer T, Townsend DW, Brasse D. Evaluation of clinical PET count rate performance. IEEE Trans Nucl Sci. 2003;50:1379–85.
4. Lartizien C, Comtat C, Kinahan PE, Ferreira N, Bendriem B, Trebossen R. Optimization of injected dose based on noise equivalent count rates for 2- and 3-dimensional whole-body PET. J Nucl Med. 2002;43:1268–78.
5. Visvikis D, Fryer T, Downey S. Optimisation of noise equivalent count rates for brain and body FDG imaging using gamma camera PET. IEEE Trans Nucl Sci. 1999;46:624–30.
6. Dekemp R, Caldwell C, Farncombe T, Mckee B, Wassenaar R, Wells R, et al. PET imaging standards and quality assurance for the multi-center trials of the Ontario Clinical Oncology Group (OCOG). J Nucl Med Meet Abstr. 2006;47:365.
7. Mizuta T, Senda M, Okamura T, Kitamura K, Inaoka Y, Takahashi M, et al. NEC density and liver ROI S/N ratio for image quality control of whole-body FDG-PET scans: comparison with visual assessment. Mol Imaging Biol. 2009;11:480–6.
8. Fukukita H, Suzuki K, Matsumoto K, Terauchi T, Daisaki H, Ikari Y, et al. Japanese guideline for the oncology FDG-PET/CT

data acquisition protocol: synopsis of Version 2.0. Ann Nucl Med. 2014;28:693–705.

9. Murayama H. Radiation detectors in positron emission tomography. Med Imaging Technol. 2000;18:15–23 (in Japanese with English abstract).

10. Barton JB, Hoffman EJ, Iwanczyk JS, Dabrowski AJ, Kusmiss JH. A high resolution detection system for positron tomography. IEEE Trans Nucl Sci. 1983;30:671–5.

11. Tarantola G, Zito F, Gerundini P. PET instrumentation and reconstruction algorithms in whole-body applications. J Nucl Med. 2003;44:756–69.

12. National Electrical Measurements Association. Performance measurements of positron emission tomographs. NEMA Standards Publication NU 2-2007. Rosslyn: NEMA; 2007.

13. Wagatsuma K, Miwa K, Miyaji N, Murata T, Umeda T, Osawa A, et al. Comparison of (18)F-fluoro-2-deoxy-D-glucose positron emission tomography/computed tomography image quality between commercial and in-house supply of FDG radiopharmaceuticals. Jap J Radiol Technol. 2014;70:339–45 (in Japanese with English abstract).

14. Shimada N, Daisaki H, Murano T, Terauchi T, Shinohara H, Moriyama N. Optimization of the scan time is based on the physical index in FDG-PET/CT. Jpn J Radiol Technol. 2011;67:1259–66 (in Japanese with English abstract).

15. Brasse D, Tararine M, Lamer O, Bendriem B. Investigation of noise equivalent count rate in positron imaging using a dual head gamma camera. IEEE Trans Nucl Sci. 1998;45:438–42.

16. Surti S, Kuhn A, Werner ME, Perkins AE, Kolthammer J, Karp JS. Performance of Philips Gemini TF PET/CT scanner with special consideration for its time-of-flight imaging capabilities. J Nucl Med. 2007;48:471–80.

17. Zaidi H, Ojha N, Morich M, Griesmer J, Hu Z, Maniawski P, et al. Design and performance evaluation of a whole-body Ingenuity TF PET-MRI system. Phys Med Biol. 2011;56:3091–106.

18. Osawa A, Miwa K, Wagatsuma K, Takiguchi T, Tamura S, Akimoto K. Relationship between image quality and cross-sectional area of phantom in three-dimensional positron emission tomography scan. Jpn J Radiol Technol. 2012;68:1600–7 (Japanese with English abstract).

19. Ferrero A, Poon JK, Chaudhari AJ, MacDonald LR, Badawi RD. Effect of object size on scatter fraction estimation methods for PET—a computer simulation study. IEEE Trans Nucl Sci. 2011;58:82–6.

20. Konik A, Madsen MT, Sunderland JJ. GATE simulations of human and small animal PET for determination of scatter fraction as a function of object size. IEEE Trans Nucl Sci. 2010;57:2558–63.

21. Constantinescu CC, Mukherjee J. Performance evaluation of an Inveon PET preclinical scanner. Phys Med Biol. 2009;54:2885–99.

22. Agostinelli S, Allison J, Amako K, Apostolakis J, Araujo H, Arce P, et al. Geant4—a simulation toolkit. Nucl Instrum Methods A. 2003;506:250–303.

23. Allison J, Amako K, Apostolakis J, Araujo H, Dubois PA, Asai M, et al. Geant4 developments and applications. IEEE Trans Nucl Sci. 2006;53:270–8.

24. Lo Meo S, Cicoria G, Campanella F, Mattozzi M, Panebianco AS, Marengo M. Radiation dose around a PET scanner installation: comparison of Monte Carlo simulations, analytical calculations and experimental results. Phys Med. 2014;30:448–53.

25. Meo SL, Bennati P, Cinti MN, Lanconelli N, Navarria FL, Pani R, et al. A Geant4 simulation code for simulating optical photons in SPECT scintillation detectors. J Inst. 2009;. doi:10.1088/1748-0221/4/07/P07002.

26. Schneider W, Bortfeld T, Schlegel W. Correlation between CT numbers and tissue parameters needed for Monte Carlo simulations of clinical dose distributions. Phys Med Biol. 2000;45:459–78.

27. Daube-Witherspoon ME, Karp JS, Casey ME, DiFilippo FP, Hines H, Muehllehner G, et al. PET performance measurements using the NEMA NU 2-2001 standard. J Nucl Med. 2002;43:1398–409.

28. Daube-Witherspoon ME, Muehllehner G. Treatment of axial data in three-dimensional PET. J Nucl Med. 1987;28:1717–24.

29. International Committee on Radiation Units and Measurements. Photon, electron, proton, and neutron interaction data for body tissues (ICRU Report 46), Bethesda; 1992.

30. Ay MR, Sarkar S. Computed tomography based attenuation correction in PET/CT: principles, instrumentation, protocols, artifacts and future trends. Iran J Nucl Med. 2007;15:1–29.

31. Watson CC, Casey ME, Bendriem B, Carney JP, Townsend DW, Eberl S, et al. Optimizing injected dose in clinical PET by accurately modeling the counting-rate response functions specific to individual patient scans. J Nucl Med. 2005;46:1825–34.

32. Oka R, Miura K, Sakurai M, Nakamura K, Yagi K, Miyamoto S, et al. Impacts of visceral adipose tissue and subcutaneous adipose tissue on metabolic risk factors in middle-aged Japanese. Obesity. 2010;18:153–60.